Received <day> <Month>, <year>; | Revised <day> <Month>, <year>; | Accepted <day> <Month>, <year>

DOI: xxx/xxxx

RESEARCH ARTICLE

Study of the interaction between dry granular flows and rigid barriers with an SPH model

Xuzhen He[1] | Dongfang Liang[2] | Wei Wu*[1] | Guoqing Cai[3] | Chenggang Zhao[3] | Shun Wang[1]

[1]Institut für Geotechnik, Universität für Bodenkultur, Wien, Austria
[2]Department of Engineering, University of Cambridge, Cambridge, UK
[3]Department of Geotechnical Engineering, Beijing Jiaotong University, Beijing, China

Correspondence
*Wei Wu, Institut für Geotechnik, Universität für Bodenkultur, Wien, 1180, Austria. Email: wei.wu@boku.ac.at

Abstract

This study uses an incompressible Smoothed-Particle Hydrodynamics (SPH) model to investigate the interaction between dry granular material flows and rigid barriers. The primary aim is to summarise some practical guidelines for the design of debris-resisting barriers. The granular materials are modelled as a rigid-perfectly plastic material where the plastic flow corresponds to the critical state. The coupled continuity equation and momentum equation are solved by a semi-implicit algorithm. Compared with flows in controlled flume experiments, the model adequately reproduces both the kinetic of the flows and the impact force under various conditions. Then, the numerical simulations are used to study the detailed interaction process. It is illustrated quantitatively that the interaction force consists of two parts, i.e. the earth pressure force caused by the weight of the soil and a dynamic force caused by the internal deformation (flowing mass on top of a dead zone). For the estimation of impact load, this study suggests that an increased earth pressure coefficient depending on the Froude number should be incorporated into the hydrostatic model.

KEYWORDS:
Incompressible SPH, Mohr-Coulomb model, Landslides, Barriers, Impact load

1 | INTRODUCTION

In earlier studies of landslides, efforts were mainly devoted to studying the triggering mechanisms of landslides and to developing techniques to stabilise slopes based on the understanding of the failure mechanisms. For some large cities, which have high population density and lie close to natural hillsides, preventive works may prove to be extensive and costly. Passive mitigation measures may then be a cost-effective solution. A rigid debris-resisting barrier is one of the most commonly-used passive measures to mitigate natural terrain landslides. Before the design of such a barrier, the possible run-up of landslides must be estimated to prevent from over-spilling and the interaction load likely to be exerted on it has also to be determined (Figure 1 a).

In practice, there are two empirical models to calculate the impact force. The hydrostatic approach (Figure 1 b) assumes a triangular load distribution and the maximum pressure is taken to be the product of an empirical coefficient, the bulk density and the run-up (1). This empirical coefficient was measured between 0.2 and 2 on real-scale experiments by (2). The hydrodynamic approach (Figure 1 c) assumes a constant load distribution, of which the pressure has a linear relationship with the square of impact velocity and the bulk density (3). Both models are over-simplified. In fact, the flow pattern is rather complex involving a dead zone which gives a static load and flowing layers which have a dynamic impact load. As a consequence, the estimated empirical coefficient varies greatly in laboratory or real-scale experiments (2). (4) suggested that the impact force is a combination of three sources: the force generated by the dead zone, a passive earth pressure and a drag force. They tried to study

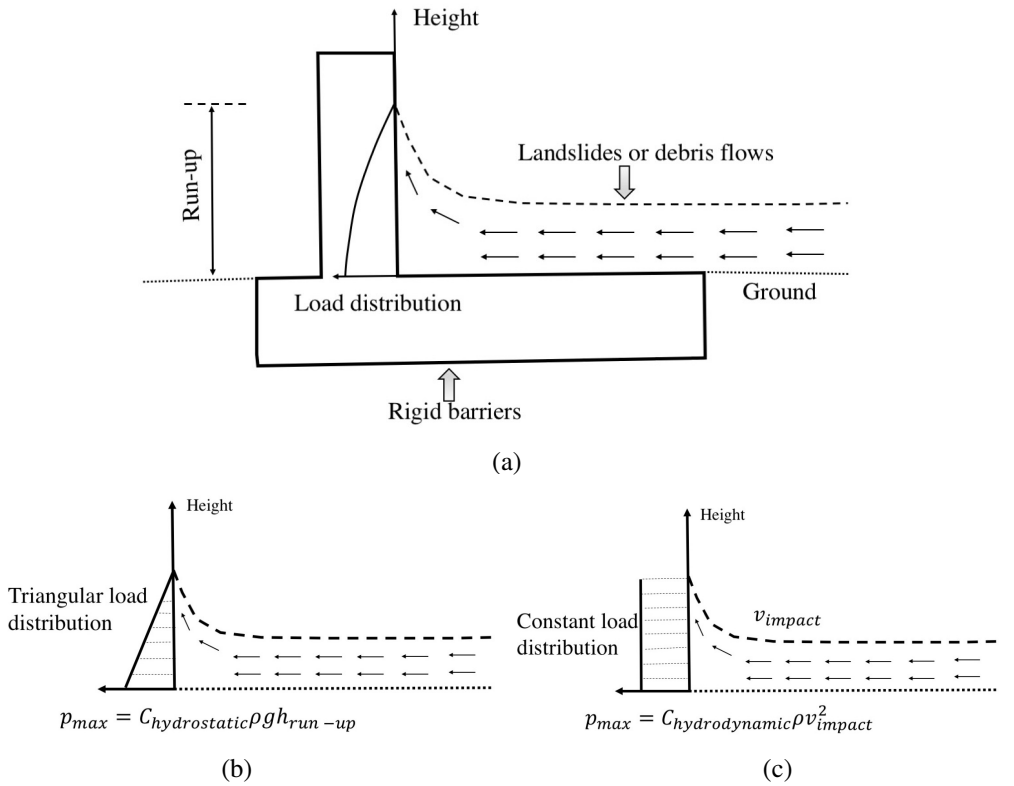

FIGURE 1 Empirical models to estimate the impact load. (a) design of debris-resisting barriers. (b) hydrostatic model. (c) hydrodynamic model.

this with measurement of dry granular flows in flumes. However, due to the limited accuracy of the experimental instruments, the three different sources can only be roughly estimated at several time snaps. In addition, some parameters such as the static friction angle to calculate the force contributed by the dead zone could not be measured directly in experiments. In contrast, the physical quantities of interest could be calculated straightforwardly in numerical simulations and used for analysis.

With the development of computing techniques and mathematical models, a number of numerical methods have been used in the study of this problem. The discrete element method (DEM) was applied to study the interaction between granular flows and obstacles, and also the efficiency of different obstacle configurations in dissipating the kinetic energy of granular flows (5). However, the DEM is a numerical method to study the bulk behaviour of granular materials by modelling the motion of each grain and the contact between grains. To obtain results matching physical experiments, it is difficult to calibrate the parameters. Also, in most engineering application with DEM, the scale-length of the problem and the scale-length of the grain-size cannot both be preserved. Therefore, either a reduced problem is studied or grains with larger size are used to represent the material. The finite volume method (6) extensively used in fluid dynamic problems has also been used in the prediction of dry granular flows and the estimation of impact forces. This grid-based Eularian method is relatively computing power demanding. Additionally, grid-based methods with Lagarangian description could suffer from grid distortion which will lead to the inaccuracy of solution or even failure of computation. Some hybrid numerical methods combining particles and mesh/grid are also developed and used in geotechnical problems (7, 8). The SPH numerical method is a pure mesh-free method. its Lagarangian description has an advantage in this kind of long-displacement problems that the computation is only done at places where there is any material. Therefore, the computation is less time-consuming. Efforts have been made to implement soil mechanics models in the SPH method to study slope stability (9), large deformations of soils (10, 11) and soil-water-interaction problems (12). (13) approximated the reduced shallow-water equations for dry soils with SPH techniques and studied the run-out of landslides in three-dimensional space. However, because their model is based on reduced equations which ignore the variation along the direction perpendicular to the bed, it might not be suitable for the study of interaction problems. The incompressible SPH was recently used to simulate the flow of granular materials and to study the run-out (14, 15). However, this method has not been used to study the interaction between dry granular materials and rigid barriers and the estimation of impact forces.

2 | MATHEMATICAL MODEL

The soil usually exhibits complex volumetric change under various loading conditions (17) and the observed dilatancy phenomena is unique to granular materials (18). The dilatancy also plays an important role in the analysis of slope stability (19). However, in the interaction problems between dry granular flows and structures, the soil elements should stay in a critical state where the dilatancy is zero (20) and the ignorance of the dilatancy in this study should not introduce much error. Additionally, even the constitutive model accounts for the compressibility, the majority of existing numerical models can not satisfactorily reproduce the desired compressible behaviour due to numerical errors (21, 11). Therefore, in the present study, the dry granular mass is modelled as an incompressible material with the governing equations as follows.

$$\frac{d\rho}{dt} = -\rho\nabla\cdot\boldsymbol{v} = 0 \tag{1}$$

$$\frac{d\boldsymbol{v}}{dt} = \frac{1}{\rho}\nabla\cdot\boldsymbol{\sigma} + \boldsymbol{g} = -\frac{1}{\rho}\nabla p + \frac{1}{\rho}\nabla\cdot\mathbf{s} + \boldsymbol{g} \tag{2}$$

Here, $\rho = \frac{\rho_{solid}}{1+e}$ is the bulk density of the soil, with ρ_{solid} and e the density of the solid and the void ratio, respectively. During flow, the density of solid and the void ratio are assumed to be constants to meet the incompressible condition. $\boldsymbol{\sigma}$ is the stress tensor. p is the mean stress or the pressure. $\mathbf{s}$ is the deviatoric stress tensor. $\boldsymbol{g}$ is the acceleration due to gravity.

2.1 | Incompressible SPH

Readers are referred to (22) , (23) , (11) and (16) for the basis of SPH such as the smoothing kernels, the kernel approximation, the particle approximation, etc. Here, we focus on introducing the different part of our incompressible SPH Scheme. The present study chooses the quintic Wendland smoothing kernel $W(\boldsymbol{x}, h)$ (24), where h denotes the smoothing length and $\boldsymbol{x}$ denotes the position vector. For two neighbouring particles at positions $\boldsymbol{x}^a$ and $\boldsymbol{x}^b$ respectively, the short notations $W^{ab} = W(\boldsymbol{x}^a - \boldsymbol{x}^b, h)$ and $\nabla W^{ab} = \nabla W(\boldsymbol{x}^a - \boldsymbol{x}^b, h)$ are used.

The incompressible SPH was firstly used by (33) for the study of free-surface flows and then improved and used in various hydrodynamic problems (25, 34). In the simulations, the velocity $\boldsymbol{v}_i$ should be a divergence-free field due to the incompressible assumption. The governing continuity and momentum equations are then solved simultaneously with a projection method (25), in which a predictor step and a corrector step are used to march the particles from time t^n to time $t^{n+1} = t^n + \Delta t$. In the following equations, the symbols $f^{a,n}$ and $f^{a,n+1}$ denote the values of a function f at particle a at time t^n and time t^{n+1}, respectively. If the time step index is omitted in an equation, then the values are all evaluated at the same time step.

The predictor step is the integration of the momentum equation in time considering only the gravity term and deviatoric stress term. The intermediate velocity is calculated as:

$$\frac{\boldsymbol{v}^{a,n*} - \boldsymbol{v}^{a,n}}{\Delta t} = \sum_b^{N_{nei}} m^b\left(\frac{\mathbf{s}^{a,n}}{(\rho^a)^2} + \frac{\mathbf{s}^{b,n}}{(\rho^b)^2}\right)\nabla W^{ab,n} + \boldsymbol{g} \tag{3}$$

Here, f^{n*} denotes the intermediate value when marching from t^n to t^{n+1}. N_{nei} denotes the set of particles who are the neighbours of particle a. In the predictor step, the continuity equation is not considered. Then a corrector step is used to adjust the intermediate velocity by taking into account the pressure gradient term.

$$\frac{\boldsymbol{v}^{a,n+1} - \boldsymbol{v}^{a,n*}}{\Delta t} = -\sum_b^{N_{nei}} m^b\left(\frac{p^{a,n+1}}{(\rho^a)^2} + \frac{p^{b,n+1}}{(\rho^b)^2}\right)\nabla W^{ab,n} \tag{4}$$

In Equations 3 and 4, the SPH techniques are used to estimate the gradient of pressure and deviatoric stress. The following Poisson equation should be used to calculate the pressure field, which will generate the correct pressure gradient term in Equation 4 to ensure the conservation of mass at t^{n+1}. The pressure is calculated from a system of linear equations constructed by the Poisson equation and the coefficient matrix is a sparse matrix.

$$[\nabla\cdot(\frac{1}{\rho}\nabla p)]^{a,n+1} = \sum_b^{N_{nei}} m^b \frac{8}{(\rho^a+\rho^b)^2}\frac{p^{a,n+1} - p^{b,n+1}}{(\boldsymbol{r}^{ab,n})^2 + \eta^2}[\boldsymbol{x}^{ab}\cdot\nabla W^{ab,n}] = \frac{\rho^{a,n} - \rho^{a,n*}}{\rho^{a,n}\Delta t^2} \tag{5}$$

Here, η is a small value, taken to be $0.1h$, to keep the denominator non-zero even if two particles are very close. $\boldsymbol{r}^{ab,n}$ is $|\boldsymbol{x}^{a,n} - \boldsymbol{x}^{b,n}|$. In Equation 5, the intermediate density is approximated to be $\rho^{a,n*} = \sum_b^{N_{nei}} m^b W^{ab,n*}$, whereas the initial density is estimated

to be $\rho^{a,n} = \sum_b^{N_{nei}} m^b W^{ab,n}$. In this SPH method, there is no need for the introduction of any sound speed. Hence, the Courant criterion is based on the particle velocities rather than the wave speed, which allows a bigger time step than other explicit SPH models (11, 9).

$$\Delta t \leq C_{max} \frac{\Delta l}{|\boldsymbol{v}|_{max}} \tag{6}$$

Here, $|\boldsymbol{v}|_{max}$ is the maximum velocity, Δl is the initial spacing of particles, C_{max} is the Courant number and 0.1 is found to be an appropriate value for C_{max} in the present simulations. Additionally, the stress predicted by this semi-implicit method is also relatively stable compared with other explicit SPH models (14). Therefore, this method is suitable for the interaction problems where the stress is of great interest.

2.2 | Strain Rate

In the literature, the strain rate in SPH models are usually estimated by Equation 7 below (11, 9), where the gradient of velocity is estimated by the conventional SPH techniques.

$$\dot{\boldsymbol{\varepsilon}}^a = \frac{1}{2} \sum_b^{N_{nei}} \frac{m^b}{\rho^b} [(\boldsymbol{v}^b - \boldsymbol{v}^a) \otimes \nabla W^{ab,n} + \nabla W^{ab,n} \otimes (\boldsymbol{v}^b - \boldsymbol{v}^a)] \tag{7}$$

However, Equation 7 does not even have first order accuracy due to particle inconsistency and the accuracy is severely reduced near boundaries due to particle deficiency (23). Figure 2 c ∼ d shows the errors of SPH-calculated strain rate tensor compared with the analytical results in a square domain with length $L = 0.02$ m. Particles are generated randomly with a spacing of $L/20$. We assume a velocity field on these particles with velocities only in the x direction and with a velocity profile $v_x = \frac{v_{max}}{L}(2Ly - y^2)$(Figure 2 a). This is a typical velocity profile for a Newtonian fluid flowing on a slope when the steady state is achieved. The slope can be seen as on the x axis with the positive x direction as the direction of flow. L can be seen as the thickness of the Newtonian fluid current. The velocity is zero on the x axis and increases with y. It reaches its maximum $v_{max} = 1$ m/s at $y = L$. Therefore, the analytical deviatoric strain rate can be calculated through definition and one has $(\dot{\epsilon}_{xy})_{analytical} = \frac{v_{max}}{L^2}(L - y)$ (Figure 2 b). It is at its maximum $\frac{v_{max}}{L}$ on the x axis and decreases linearly with y. It reaches zero at $y = L$.

The error of the magnitude of the deviatoric strain rate (Figure 2 c) is measured as $\lambda = \frac{(\dot{\epsilon_{xy}})_{SPH} - (\dot{\epsilon}_{xy})_{analytical}}{[(\dot{\epsilon}_{xy})_{analytical}]_{max}}$. $(\dot{\epsilon_{xy}})_{SPH}$ is the calculated SPH approximation at every particle and $(\dot{\epsilon}_{xy})_{analytical}$ is the analytical strain rate. The error of the principal directions (Figure 2 d) is measured as $\theta_d = \theta_{SPH} - \theta_{analytical}$. θ denotes the angle between the principal directions and x axis. θ_{SPH} is the angle calculated from SPH approximations and $\theta_{analytical}$ is the angle from the analytical strain rate tensor.

Figure 2 c and 2 d are errors calculated by Equation 7 . This clearly shows that this SPH approximation is less than second order accurate because the analytical strain rate tensor is an exact linear field. Most importantly, the errors near boundaries are greater than the ones of interior particles due to particle deficiency. Actually, the calculated strain rate of particles near the x axis is only 44% of the analytical value. When estimating the strain rate tensor, ghost or dummy particles outside boundaries with reflected velocities along boundaries were used to avoid particle deficiency and to improve the accuracy near slip-free boundaries (11, 10).

In this study, the corrected gradient of the kernel is used for the estimation of strain rate to improve the accuracy, as expressed below:

$$\dot{\boldsymbol{\varepsilon}}^a = \frac{1}{2} \sum_b^{N_{nei\_ex}} \frac{m^b}{\rho^b} [(\boldsymbol{v}^b - \boldsymbol{v}^a) \otimes \widetilde{\nabla} W^{ab,n} + \widetilde{\nabla} W^{ab,n} \otimes (\boldsymbol{v}^b - \boldsymbol{v}^a)] \tag{8}$$

One thing to note is that the summation is conducted over N_{nei_ex}, which is the set of neighbouring particles excluding dummy particles (explained below). Here, $\widetilde{\nabla} W^{ab,n} = \mathbf{B}^{-2,a} \nabla W^{ab,n}$ and $\mathbf{B}^{-2,a}$ is the inverse of $\mathbf{B}^{2,a} = \sum_b^{N_{nei\_ex}} \frac{m^b}{\rho^b} (\boldsymbol{x}^b - \boldsymbol{x}^a) \otimes \nabla W^{ab,n}$. $\widetilde{\nabla} W^{ab,n}$ is termed as the corrected gradient of kernel (26).

Figure 2 e and 2 f show the errors of Equation 8 for the same particle configuration and velocity profile. It can be seen that this equation improves the accuracy and also obtains much more reliable results for particles near boundaries. However, this equation is also less than second order accurate and can not exactly reproduce a linear strain rate field.

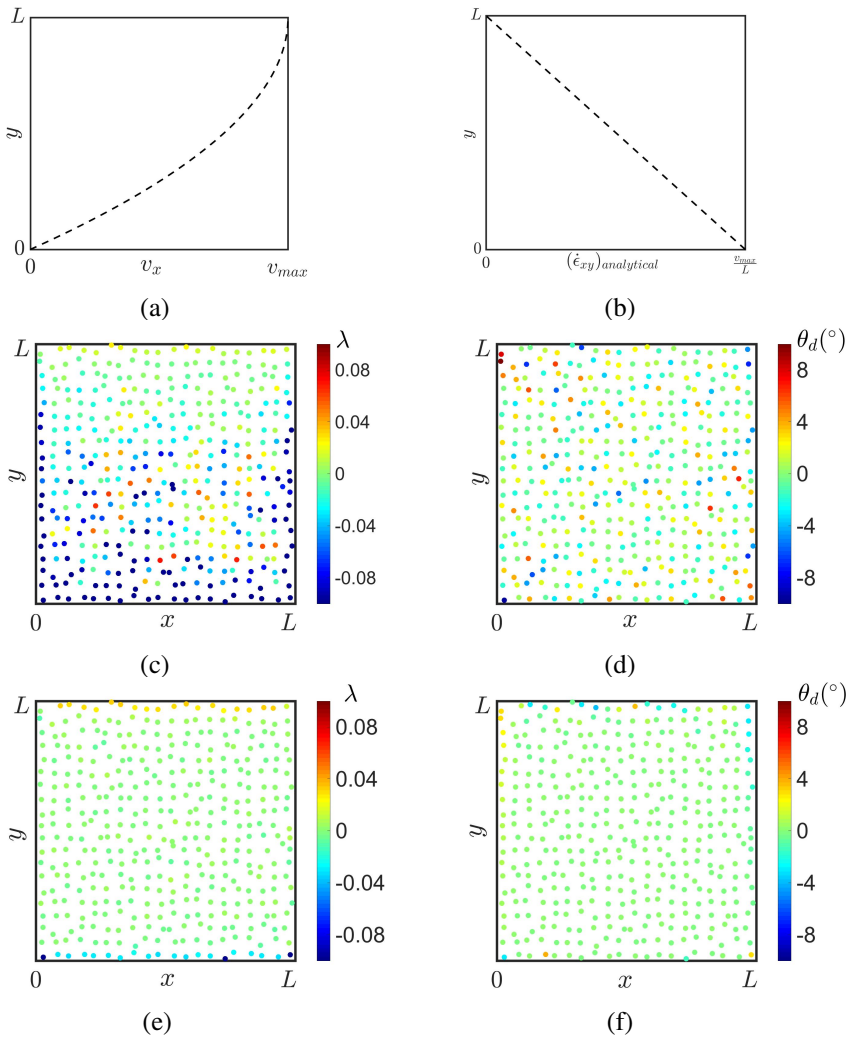

FIGURE 2 Error of the SPH-estimated strain rate tensor. (a) velocity profile. (b) analytical strain rate. (c)∼(d) Equation 7 . (e)∼(f) Equation 8 . (c) and (e) error of magnitude. (d) and (f) error of principal direction.

2.3 | Mohr-Coulomb Model

There have been extensive research on the mechanics of granular materials. During the mobilisation stage, the evolution of the frictional resistance and dilatancy depends on the initial state of the soil (18). After a so-called critical state is reached after large deformations, however, the coefficient of friction resistance remains constant and the dilatancy becomes zero (20). In the interaction problem between dry granular flows and barriers, the flowing mass should stay in a critical state. Therefore, in this study, the soil is modelled as a rigid-perfectly plastic material where the plastic flow corresponds to the flow at a critical state. This model has one advantage over the incremental constitutive models (9) that the stress is determined directly from the yield criteria and this guarantees that the stress is always on the yield surface. The Coulomb yield criterion assumes that, on the failure plane (F in Figure 3), the shear stress τ and the effective normal stress σ' have the following relationship.

$$\tau = \sigma' \tan\phi_{crit} \tag{9}$$

where ϕ_{crit} is the internal friction angle, chosen as the critical state value to match the plastic flow with the critical state. In plane-strain problems, the deviatoric stress is $|\mathbf{s}| = (\sigma'_1 - \sigma'_3)/2$ and the mean stress is $p = (\sigma'_1 + \sigma'_3)/2$. Here, σ'_1 and σ'_3 are the effective principal stresses. It is easy to verify that $|\mathbf{s}| = p \sin\phi_{crit}$, which is often referred to as the Drucker-Prager yield

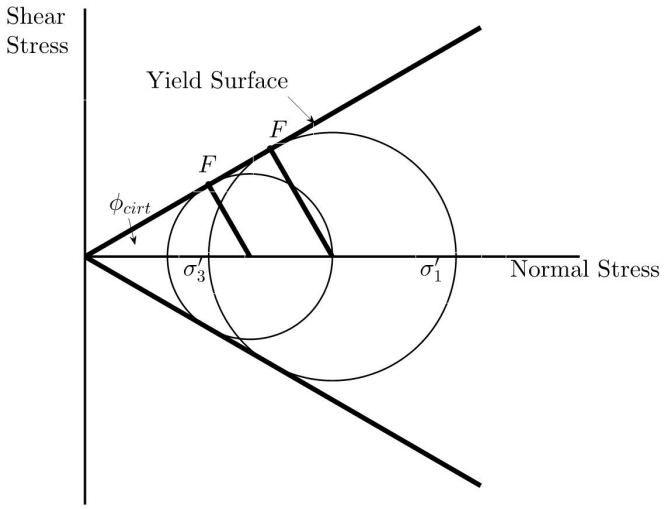

FIGURE 3 Mohr diagram showing the Coulomb yield surface.

criterion (20). Studies show that the stress tensor and strain rate tensor are coaxial at the critical state in simple shear flows (27) and transient flows (28). With such a coaxial assumption, the following equation is used to calculate the deviatoric stress tensor.

$$\mathbf{s} = p \sin\phi_{crit} \frac{\dot{\boldsymbol{\epsilon}}}{|\dot{\boldsymbol{\epsilon}}|} \tag{10}$$

Here, $\dot{\boldsymbol{\epsilon}}$ the deviatoric strain rate tensor. In SPH, this equation is implemented in the predictor step. The strain rate tensor for every particle is firstly estimated using Equation 8 and the deviatoric stress tensor is updated using Equation 10.

2.4 | Free Surface

The free surface condition is implemented on a set of the most outlying particles. In (25)'s treatment, the pressure of free surface particles is assigned as zero when solving the Poisson equation and no special treatment is implemented for the momentum equations. It is found in (16) that due to the particle deficiency (23) in the SPH evaluation of the gradient of stress (Equations 3 and 4), particles near the free surface will cluster together. (16) also proposed a treatment that the pressure of free surface particles could be assigned to a small value of $\rho g \Delta l/4$, which will shift the calculated pressure field by this value, but will have no influence on the estimation of the gradient of stress for interior particles. This treatment is used in the present study. The free surface particles are tracked based on the knowledge that their SPH estimation of density drops abruptly due to particle deficiency. The criterion used for the detection of free surface particles is $\rho^{a,n} < 0.97\rho^0$ (25, 33).

2.5 | Fixed Boundary

At the fixed boundary, a non-penetration Coulomb friction condition is usually adopted (13). In this study, one layer of boundary particles is placed on the boundary (solid black dots in Figure 4 a) and several layers of dummy particles (crosses in Figure 4 a) are placed outside the boundary.

During calculations, the velocity and position of boundary particles and dummy particles are not updated. The pressure of boundary particles is calculated through the Poisson equation. As for the dummy particles, it has an associated boundary particle which is the closest to it among all boundary particles. The stress on this dummy particle is specified to be the same as the stress on its associated boundary particle. The non-penetration condition is achieved implicitly from the Poisson equation because the pressure at boundary particles is able to repel the approaching soil particles to avoid particle penetration.

The Coulomb friction condition is achieved by applying an equation similar to Equation 10 (the wall friction coefficient μ_w is used instead of the internal friction coefficient) to update the deviatoric stress of boundary particles. However, this implementation is correct only when the velocity of particles close to the boundary is perfectly along the tangential. Actually, this is only

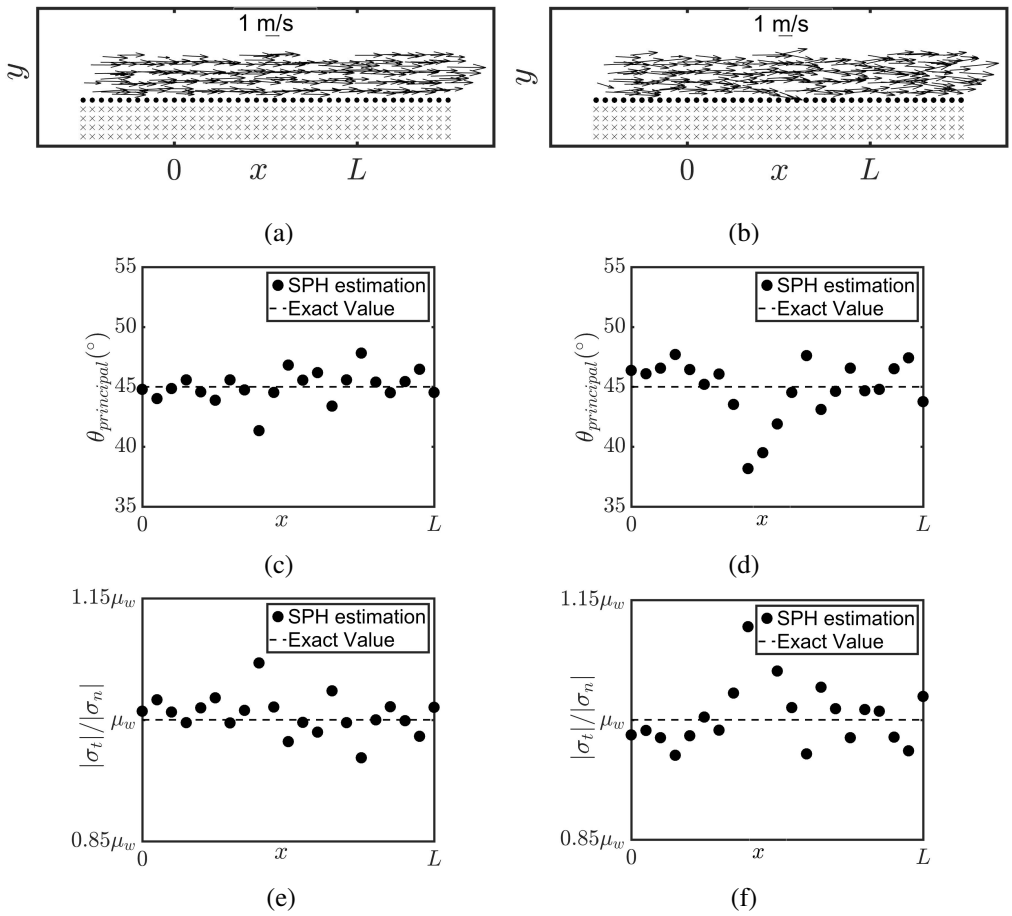

FIGURE 4 Accuracy of the Coulomb boundary condition for two test cases. Left: standard deviation $0.1v_{ave}$. Right: standard deviation $0.3v_{ave}$. (a)~(b) velocity. (c)~(d) SPH-estimated principal direction. (e)~(f) SPH-estimated stress ratio.

approximately achieved. Thus, two test cases are conducted to examine the accuracy if there is velocity component perpendicular to the boundary. Consider a layer of boundary particles on the x axis and several layers of soil particles above it (Figure 4 a). The spacing is $\Delta l = 1$ mm. The velocity field is generated randomly with a normal distribution. The average velocity is $\overline{v_x} = v_{ave} = 1$ m/s and $\overline{v_y} = 0$. The standard deviation for both v_x and v_y is $0.1v_{ave}$ for the test case in the left column of Figure 4 and is $0.3v_{ave}$ for the test case in the right column. The mean stress is assumed to decrease linearly with y ($p = p_0 - \rho g y$, $p_0 = 1$ kPa). Since the boundary is along the x axis, the pure shear plane should be on the x axis if there is perfectly no perpendicular velocity on the boundary. Thus, the angle between the principal directions of the strain rate tensor and the x axis should be 45°. Figure 4 c and 4 d show this angle calculated from SPH estimations for boundary particles. It can be seen that because the soil particles near the boundary have velocity toward or away from the boundary, this angle deviates from 45°. In addition, the calculated pure shear plane will be approximately along the average velocity direction of particles near the boundary. Hence, the error depends solely on the direction of the average velocity direction. The stress tensor on the boundary can also be obtained and the stress ratio is calculated and presented in Figure 4 e and 4 f. They also deviate from their actual value (the wall friction coefficient) and the deviation has an opposite trend to the deviation of principal direction.

From the test cases above, it can be concluded that the Coulomb friction condition is not exactly achieved when soil particles near the fixed boundary have velocities toward or away from the boundary. And the accuracy of the Coulomb friction condition depends on how accurately the condition of zero-velocity perpendicular to the boundary is fulfilled. However, since the average velocity in space and time will be approximately along the boundary and thus the average calculated friction coefficient in space and time will also roughly equal to the actual value.

3 | SPH-PREDICTED FLOWS AND INTERACTION FORCE

The setup to study the interaction between dry granular flows and rigid barriers is shown in Figure 5 . The granular materials are placed up a steep slope initially ($L_0 = 0.5$ m and $H_0 = 0.3$ m). The spacing Δl of SPH particles is 3.6 mm and the sand mass is discretised as 10164 SPH particles. The sand mass is unstable in the first instance and it would flow along the slope and eventually hit the rigid barrier perpendicular to the slope. The distance between the initial front and the barrier L_d is 1.8 m. The height of the barrier H_{br} is 0.3 m. Various simulations are conducted by changing the slope angle ($\alpha_s = 45°$, 50°, 55°, 60°, and 65°). A series of similar flume experiments are conducted by (6) with Toyoura sand. The bulk density of this sand is 1,379 kg/m^3 and the minimum and maximum void ratios are 0.61 and 0.97, respectively. In experiments, the flow was initiated by the the sudden lifting of a removable gate and the width of the flume W is 0.3 m. Sensors could be installed on the barrier to measure the normal impact forces.

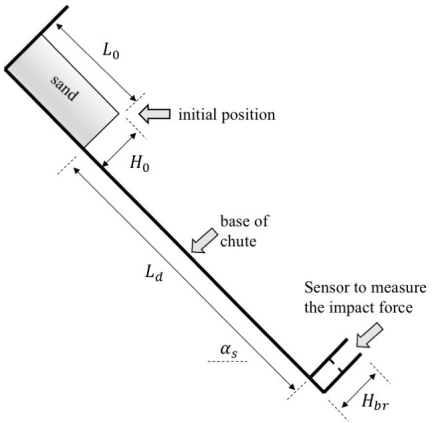

FIGURE 5 Setup to study the interaction between granular flows and rigid barriers.

3.1 | Kinetic of Flows

Figure 6 presents the velocity at four different moments from an SPH simulation and the comparison with flow mass profiles measured in experiments. The slope angle α_s is 45° and ϕ_{crit} is chosen as 44° in this simulation. The wall friction coefficient is chosen to be the same as the internal friction coefficient.

The present SPH model faithfully predicts the flow, whose feature is also illustrated by these figures. Figure 6 a shows that after the sand is released shortly, the front gains momentum quickly and the rear end is still stationary. Also, it does not move even when the front has reached the barrier (Figure 6 b). Therefore, before impact, the sand mass is very thinly spread over the slope. Figure 6 c and 6 d show the interaction and deposition process. A closer view of the predicted velocity field by SPH is also illustrated in Figure 7 a and 7 b. After the front reaches the barrier, some sand mass starts to be deposited approximately as a wedge shape in front of the barrier (Figure 7 a). This phenomenon is observed and reported by a number of researchers cornering the flow of granular materials against a obstacle with diverse configurations and this region is usually called a dead zone (4, 29, 31). Other particles would flow on top of this dead zone and the moving direction of the flowing mass seems to be diverted smoothly on the dead zone. The dead zone grows with time, at the same time, more areas of the barrier are covered with stationary sand mass. After sand reaches the edge of the barrier, the over-spilling happens (Figure 7 b).

To study the detailed interaction process using the SPH method and to give some insights into the physics in it, some quantities of interest are also recorded in the numerical method and studied below (Figure 7). The area of the dead zone is denoted as S_{dead}, the length of this zone along the barrier is $l_{br,dead}$ and the length of this zone along the chute is $l_{ch,dead}$. The height of the barrier is H_{br} and it is discretised as 84 SPH boundary particles. Because the stress on these boundary particles is calculated in SPH, if the unit normal vector of the barrier is denoted as $\boldsymbol{n}^{br}$, the normal impact force can be calculated as $N_{br} = W\Delta l \sum(\boldsymbol{n}^{br})^T \boldsymbol{\sigma} \boldsymbol{n}^{br}$. Here, $\boldsymbol{\sigma}$ is the calculated stress tensor on these boundary particles and the summation is over all these 84 boundary particles.

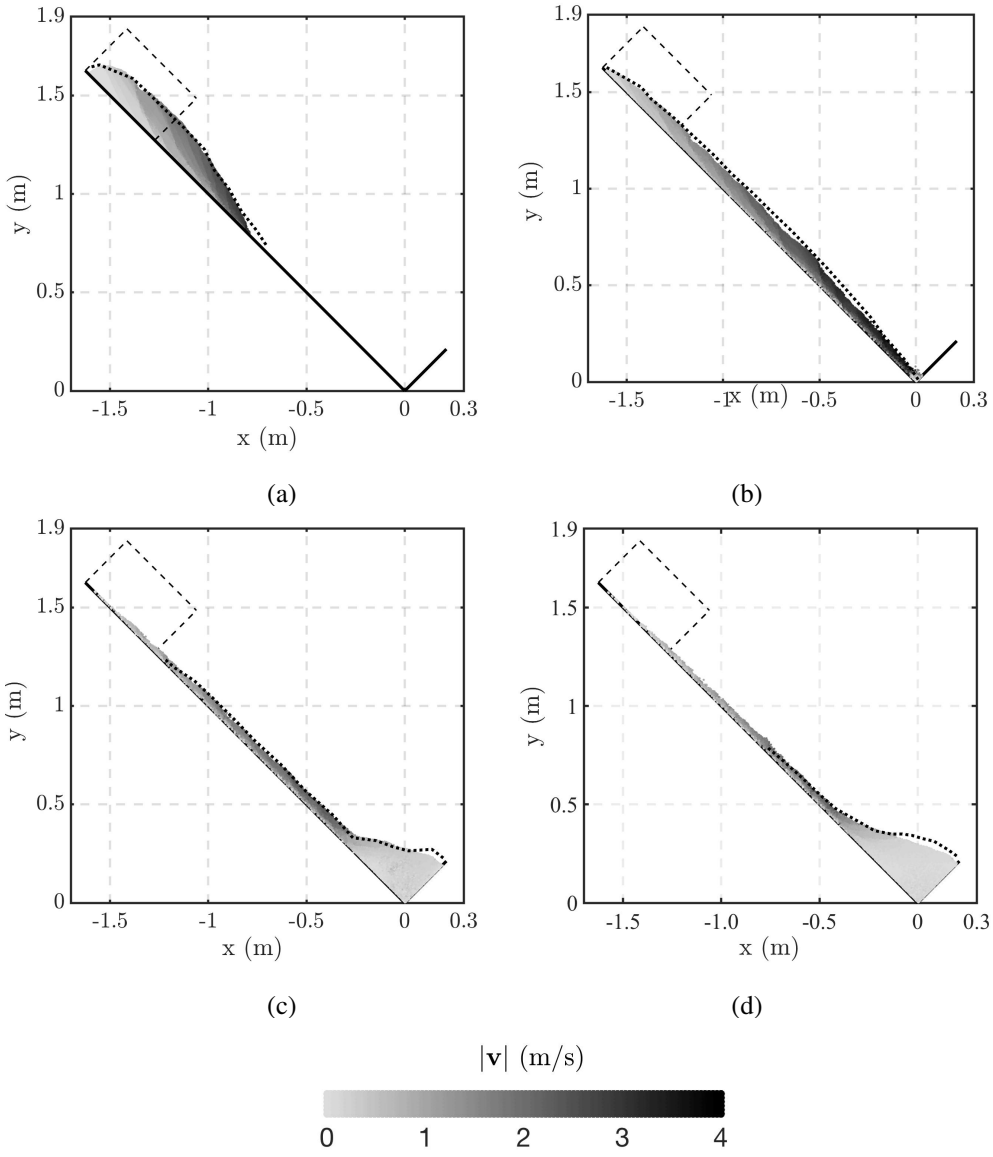

FIGURE 6 SPH-predicted kinetic of the dry granular flows (dotted lines indicate the profile in experiments by (6)). (a) t = 0.4 s. (b) t = 0.8 s (c) t = 1.2 s. (d) t = 1.6 s.

Similarly, the tangential impact force is $T_{br} = W\Delta l|\sum(\boldsymbol{\sigma}\boldsymbol{n}^{br} - [(\boldsymbol{n}^{br})^T\boldsymbol{\sigma}\boldsymbol{n}^{br}]\boldsymbol{n}^{br})|$. Defining an interaction zone as shown in Figure 7 c, the interaction forces between the sand and this section of the chute base (N_{ch} and T_{ch}) are also calculated with similar equations. This definition of interaction zone is reasonable because the sand mass outside this zone upstream the chute is flowing largely along the slope such that they actually do not 'feel' the rigid barriers ahead.

Some convergent analysis is conducted by simulating the flow on a 45° slope with various particle spacing (Δl = 1.8 mm, 2.5 mm and 3.6 mm). No noticeable difference is observed concerning the kinetic of the flow and the predicted impact force. Therefore, in subsequent simulations, the particle spacing is fixed at 3.6 mm and there are always around ten thousand soil particles. The same model has also been used in the simulation of the collapse of granular columns, the convergence rate is estimated as 1.09 in these simulations (35), which is similar to the one in hydrodynamic problems (33).

Some parameter studies are also conducted. The value of bulk density ρ in the model has no influence on the flow feature. Figure 8 a gives the deposition profiles for simulations on a 45° slope. ϕ_{crit} is chosen as 44° and three different bulk densities are used. It can be seen that the deposition profiles collapse onto each other. When different ϕ_{crit} is used, distinct flows are

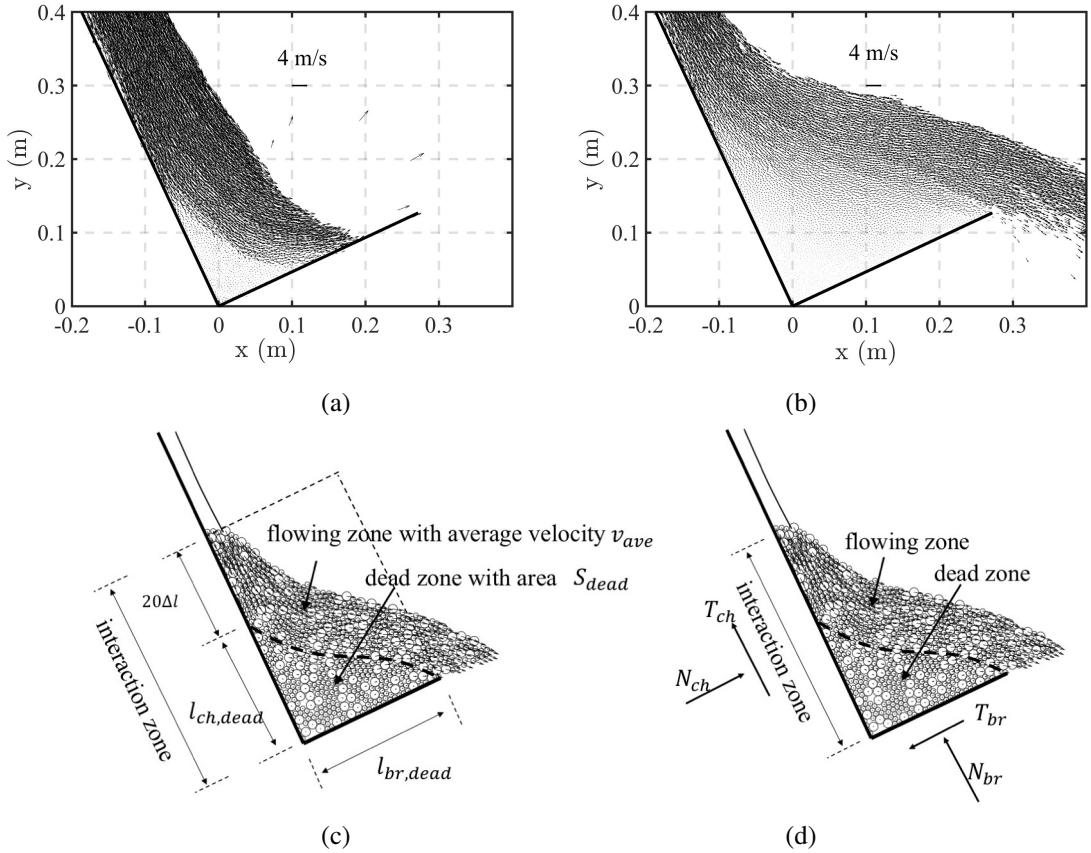

FIGURE 7 Detailed interaction process by SPH simulations and the illustration of several quantities of interest. (a) $\alpha_s = 65°$, t = 0.7 s. (b) $\alpha_s = 65°$, t = 0.9 s.

observed. For simulations again with the 45° slope, when ϕ_{crit} is chosen as 40°, a small amount of particles will overtop the barrier (circles in Figure 8 b). When ϕ_{crit} is chosen as 48°, the barrier will not be totally covered with particles (squares in Figure 8 b). In the experiment of Toyoura sand on a 45° slope, overtopping did not happen and the barrier was totally covered with sand. Therefore, 44° is a suitable value of ϕ_{crit} for the Toyoura sand and this value is used in all continuing simulations. In addition, the angle of repose (AOR) of the Toyoura sand is 33° and tan(AOR) $\approx \sin\phi_{crit}$, which happens to be consistent with the hypothesis of Roscoe (1970) for the friction angle mobilised on slip lines of zero extension and also agrees with the authors' previous study (14). Several simulations are also conducted with various wall friction angles. It is found that when the wall friction angle varies from 20° to 50° (typical values), the predicted flow is almost the same. Therefore, in the simulations in this study, the wall friction angle is chosen to be the same as the internal friction angle for simplicity.

3.2 | Interaction Force

Figure 9 gives the comparison of the normal impact force between SPH calculations and experimental measurements (6). For the time history of the normal impact force on the 45° slope (Figure 9 a), the normal force exerted on the barrier increases continuously with time after the front reaches the barrier. Additionally, the force reaches an asymptotic value after some time. The SPH model can correctly predict this but slightly overestimates the ultimate force. For steeper slopes, after the front reaches the barrier, the normal impact force increases to a peak force firstly and then decreases to an asymptotic value. The SPH model can also correctly capture this feature but overestimates the peak force. Figure 9 b compares the peak force between experimental results and SPH calculations under various slope conditions. The peak force will increase with the increase of slope angle α_s. The numerical method can capture this feature but overestimates the peak force in all slope conditions. This could be attributed to the fact that in experiments, the width of initial container is slightly smaller than the width of the flume and therefore, the

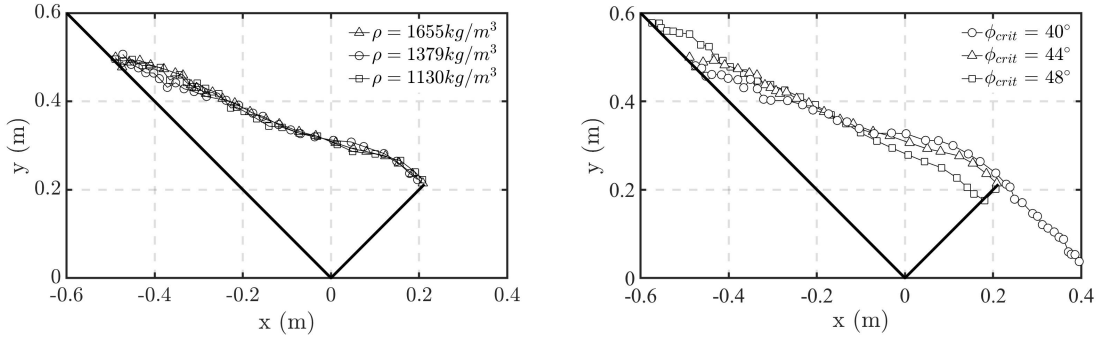

FIGURE 8 SPH-simulated deposition profiles with various model parameters.

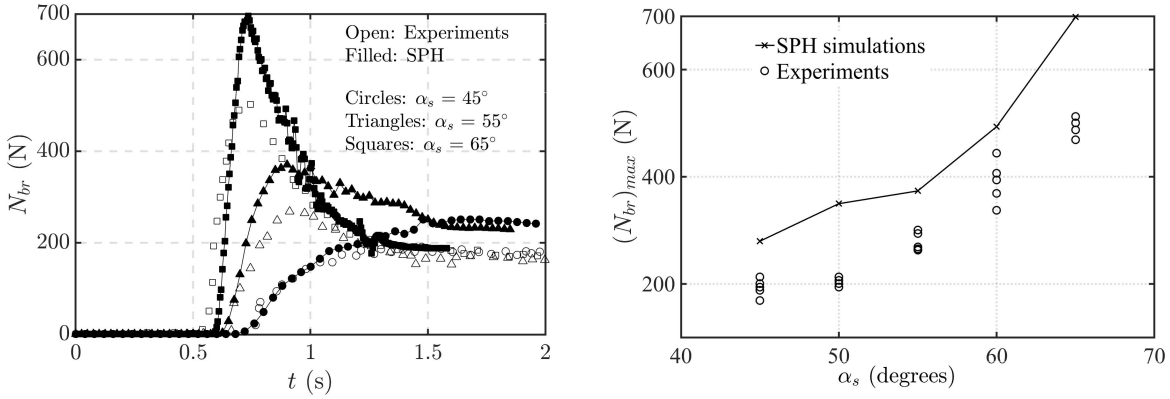

FIGURE 9 Comparison of the normal impact force from experiments and from SPH simulations.

flow is not perfectly two-dimentional. Additionally, the sand would dilate to a critical state density before being fully mobilised. Although the bulk density has no influence on the flow phenomena, the calculated impact force does have a linear relationship with it. The neglect of these effects could contribute to the inaccuracy of the predicted impact force.

Figure 10 a gives the time history of the tangential impact force T_{br} along with normal impact force on the barriers. T_{br} follows similar trend as the corresponding normal impact force. As discussed, there is always a dead zone against the barrier, and in this zone, there is no relative movement between the material and the barrier. This also means that the ratio between the tangential impact force T_{br} and normal impact force N_{br} on the barrier should always be smaller than the friction coefficient due to this dead zone. Figure 10 b gives the time history of the normal and tangential forces between the material and the chute base. Similarly, the forces exerted on the 45° slope increase continuously till an asymptotic value. For steeper slopes, the forces increase to a peak value firstly and then decrease to an asymptotic value.

4 | FINAL DEPOSITION

All the interaction forces reach an asymptotic value because part of the sand will eventually be deposited in front the barrier. And these asymptotic forces should be caused by the weight of the deposition and be in balance with the effect of gravity. Figure 11 a shows the deposition profiles at various slope conditions from SPH simulations (all profiles are moved such that the head of the barrier is at the same position). The solid lines indicate the positions of the chute bases and the barriers. It is observed that all the depositions are wedge-shaped and all the free surfaces (indicated with symbols) almost collapse onto a unique curve with

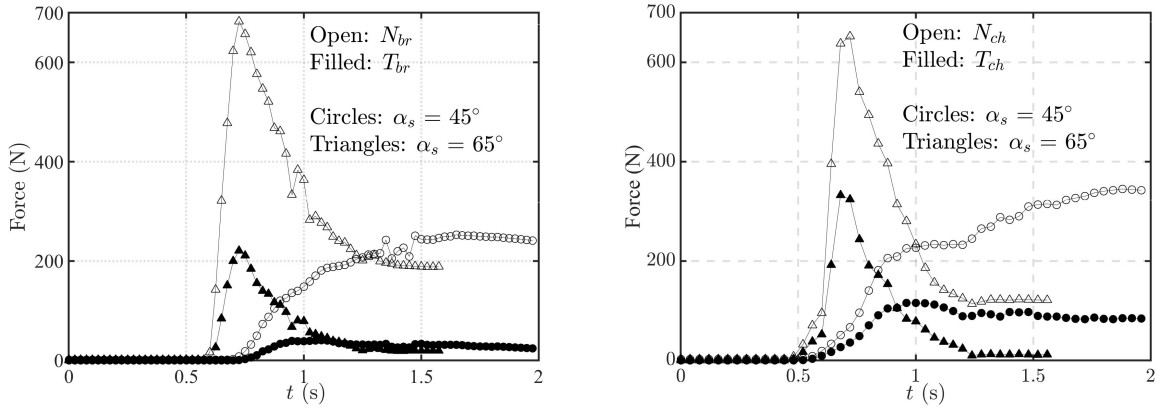

(a) (b)

FIGURE 10 Interaction forces between dry granular materials and rigid barriers.

an inclination angle of 22° to the horizontal, which is smaller than the angle of repose of the material (35°). This observation could give some implications for the design of barrier capacity that the capacity is determined by the head position of the barrier and the friction angle of the material.

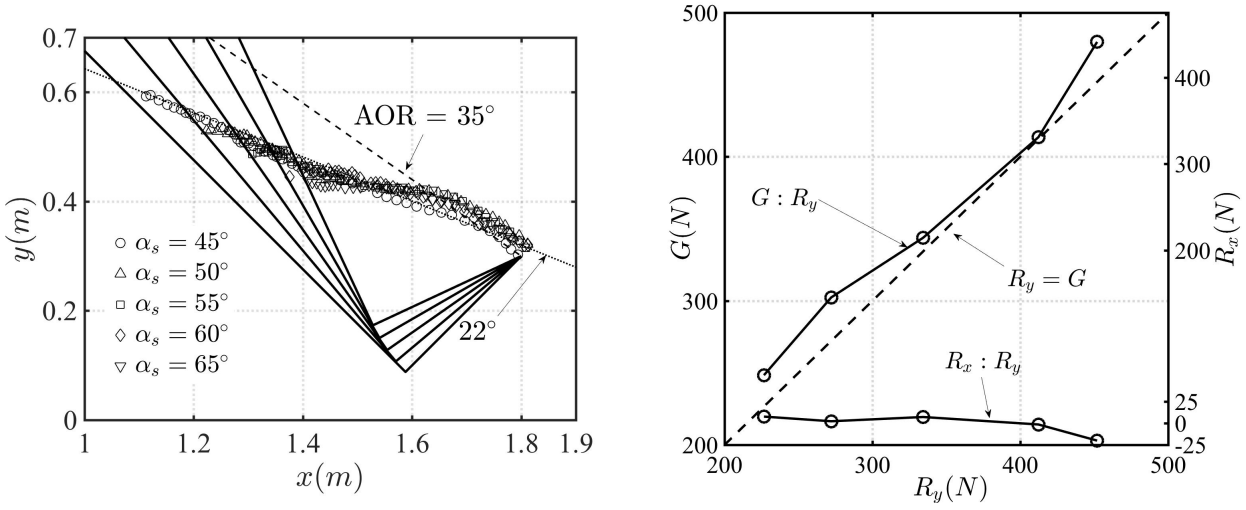

(a) (b)

FIGURE 11 Final depositions. (a) Deposition profiles. (b) Balance between the gravity and interaction forces.

The interactions forces (Table 1) should be in balance with the effect of gravity at the final deposition. To verify this, the resultant force ($\vec{R}$) of the four asymptotic interaction forces are found from Figure 10 . Its horizontal component is R_x and its vertical component is R_y. The gravity force of the final deposited mass is calculated as $G = \rho g W S_{dead,\infty}$. Figure 11 b shows the relationship between the resultant force and the gravity force. It can be seen that the horizontal component R_x is small (between -25 N and 25 N) compared with R_y (between 230 N and 450 N). And the vertical component R_y is approximately equal to the gravity force. Therefore, both the method to estimate interaction forces from SPH boundary particles and the method to estimate the weight of soil mass from the volume and density are accurate enough for this study.

Slope Angle	$N_{br,\infty}$ (N)	$T_{br,\infty}$ (N)	$\mu_{br,\infty} = \tan\phi_{br,\infty} = T_{br,\infty}/N_{br,\infty}$	$N_{ch,\infty}$ (N)	$T_{ch,\infty}$	$\mu_{ch,\infty} = \tan\phi_{ch,\infty} = T_{ch,\infty}/N_{ch,\infty}$
45°	249.3	28.6	0.115	333.9	84.4	0.253
50°	257.3	21.0	0.081	284.9	59.4	0.208
55°	232.7	20.4	0.087	218.0	37.0	0.170
60°	208.6	21.2	0.102	159.3	25.9	0.163
65°	190.7	19.2	0.100	122.0	11.4	0.094

TABLE 1 Interaction forces at final deposition.

5 | DEVELOPMENT OF DEAD ZONE AND FLOWING ZONE

The development of the dead zone and flowing zone is presented and discussed here to give some insights to the physics in the interaction. Firstly, the dead zone is growing with time, which is evidenced by Figure 12 a where the time history of the area of the dead zone S_{dead} is given. Also, S_{front}, defined as the area of all the sand in front of the rigid barrier (i.e. not over-spilt mass) is also presented. On the 45° slope, S_{front} will not change because no over-spilling will happen. For steeper slopes, S_{front} starts to decrease after some material overtops the barrier. Eventually, S_{front} is equal to S_{dead} when all the sand in front of the barrier has settled and S_{dead} grows to its ultimate value $S_{dead,\infty}$.

The shape of the dead zone is not similar at different times and the length $l_{br,dead}$ grows faster and reaches its ultimate value earlier than the length $l_{ch,dead}$ does, which is evidenced by Figure 12 b where the time history of $l_{br,dead}$ and $l_{ch,dead}$ is shown. Both lengths are normalised by their ultimate value. Clearly, the ultimate value of $l_{br,dead}$ is the height of barrier H_{br}. Based on the observation about the final deposition in Figure 11 a, the ultimate value of $l_{ch,dead}$ is approximately $L_{ch,\infty} = H_{br}\tan(22° + 90° - \alpha_s)$. Both $l_{br,dead}$ and $l_{ch,dead}$ measure the depth of the dead zone and they both increase continuously to their ultimate values. However, $l_{br,dead}$ increases to its ultimate value in a very short time interval and $l_{ch,dead}$ increases gradually. A comparison between Figure 12 b and Figure 10 leads to the observation that the peak normal impact force $(N_{br})_{max}$ happens when $l_{br,dead}$ reaches its ultimate value for the first time, which is well evidenced by the relationship between $l_{br,dead}$ and the normal impact force in Figure 12 c. In other words, the peak normal impact force and the run-up happens at the same moment, which implies that a relationship like the hydrostatic model is reasonable. However, the empirical coefficient should include the influence of dynamic effects because the estimated empirical coefficient from experiments (2) varies in a large range.

6 | DECOMPOSITION OF THE NORMAL IMPACT FORCE

Both hydrostatic and hydrodynamic models could find their physical ground. For example, as extensively addressed, there is always a stationary dead zone in front of obstacles during interaction. The earth pressure of static soil on retaining walls is linear in depth (30), therefore, the hydrostatic model is closely related to the stationary dead zone. Nevertheless, if consider the dead zone and the barrier as a whole body, which is a congregated obstacle in surrounding fluid (soil here). This is very similar to the study of drag force and the hydrodynamic model is based on this. However, the interaction process involves both. Therefore, a model accounting for both the earth pressure caused by the weight of soil and dynamic pressure of flowing soil with high kinetic energy on obstacles should be constructed to improve the prediction.

In this section, we firstly try to decompose the normal impact force into two parts. The first part is the force caused by the weight of soil $N_{br,weight}$, and the other part is the dynamic pressure force $N_{br,dyn}$ caused by the internal deformation of the flowing soil on top of a dead zone. Taking the soil mass in the interaction zone as the object (Figure 14 a), and a method similar to the Coulomb's method to calculate the lateral earth pressure is used here to estimate the interaction forces contributed only by the weight. The cross-sectional area of mass in this zone is denoted as S_{inter}. Defining $T_{br,weight}/N_{br,weight}$ as $\tan\phi_{br,weight}$

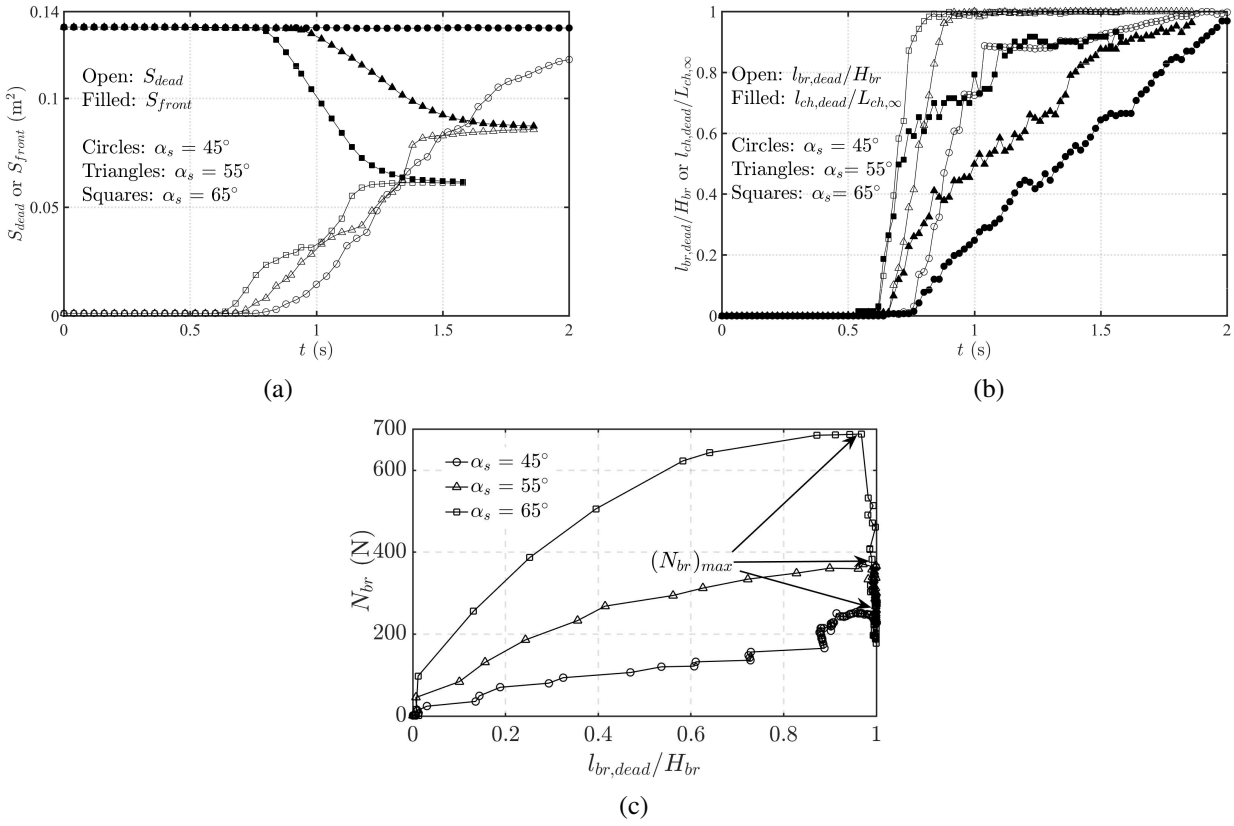

FIGURE 12 Time history of the dead zone (a) the area. (b) the length. (c) the relationship between $l_{br,dead}$ and normal impact force.

and $T_{ch,weight}/N_{ch,weight}$ as $\tan\phi_{ch,weight}$. , we can easily obtain the following equation to calculate $N_{br,weight}$ from the weight of soil (see Appendix 1).

$$N_{br,weight} = K_w \rho g W S_{inter}$$
$$K_w = \frac{\sin(\alpha_s - \phi_{ch,wehigt})\cos\phi_{br,weight}}{\cos(\phi_{ch,wehigt} + \phi_{br,weight})} \tag{11}$$

Similar to Coulomb's theory, this problem is indeterminate because $\phi_{br,wehigt}$ and $\phi_{ch,wehigt}$ are unknown and they are not equal to the friction angle on the boundaries as discussed in Section 3. However, for the final deposition, they could be calculated and are listed In Table 1 . A strong assumption is made in the present study that these angles keep constant and they are equal to the ones ($\phi_{br,\infty}$ and $\phi_{ch,\infty}$) in Table 1. Figure 13 a shows the time history of the calculated $N_{br,weight}$ from Equation 11 along with $N_{br,total}$, which is calculated from SPH boundary particles. Because we are only interested in the relative magnitude of $N_{br,weight}$ and $N_{br,total}$, the time axis for three different tests is shifted by different intervals to avoid the cluster of symbols. It can be seen that $N_{br,weight}$ increases almost continuously up to an asymptotic value which is identical to the asymptotic value of $N_{br,total}$.

The difference between these two forces is $N_{br,dyn} = N_{br,total} - N_{br,weight}$ and it is plotted in Figure 13 b with filled symbols. This dynamic component, which is caused by internal deformation, increases from zero after the front reaches the barrier and starts to decrease after the peak is reached. And it will decrease to zero when the sand mass is fully settled. We drew an analogy between the dynamic force and the drag force before. The drag force is usually formatted as $C_d \rho v^2 A/2$, where v is the velocity of fluid around obstacles, A is the cross sectional area of the obstacle and C_d is the the drag coefficient. In fluid mechanics, C_d depends on the shape of the obstacle and on the Reynolds number. Some researchers prefer to differentiate flow patterns of dry granular flows with the Froude number Fr (the ratio between inertia force and gravity) because the viscosity in the Reynolds

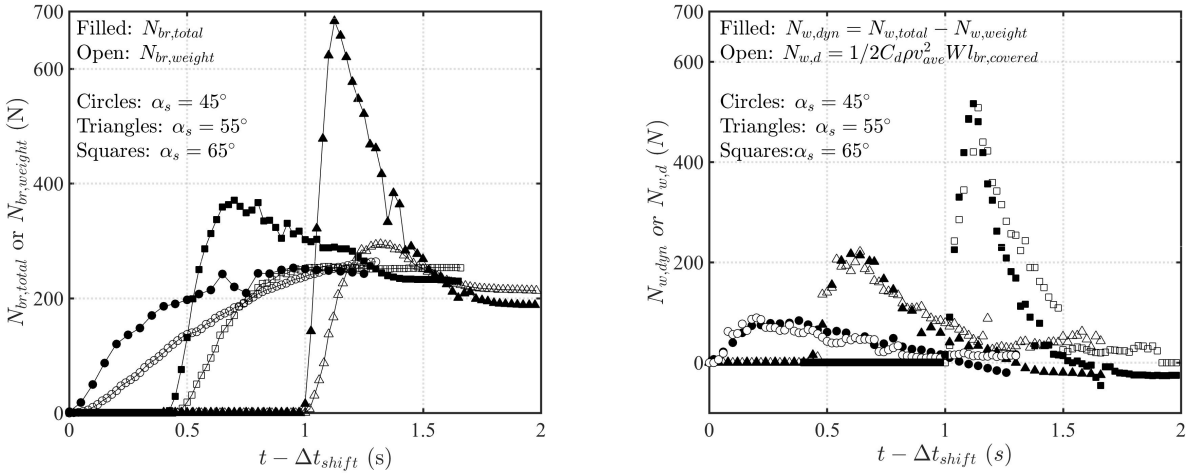

(a) (b)

FIGURE 13 Decomposition of the normal impact force. ($\alpha_s = 45°$, $\Delta t_{shift} = 0.7$ s; $\alpha_s = 55°$, $\Delta t_{shift} = 0.2$ s; $\alpha_s = 65°$, Δt_{shift} = -0.4 s;)

number is not well defined for granular materials. (4, 31, 32). In this study, we follow the trend to use the Froude number. Therefore, a similar equation is used for the dynamic interaction force of landslides on barriers as

$$N_{br,d} = \frac{1}{2} C_d \rho v_{ave}^2 W l_{br,covered}. \tag{12}$$

Here, v_{ave} during impact is estimated as the average velocity of flowing mass (i.e. not in the dead zone). $l_{br,covered}$ is the length of the barrier, which is covered with sand. Figure 13 b shows the time history of the dynamic pressure force calculated from this equation and the coefficient C_d is chosen as 1.0, 1.5 and 2.0 for the 45°, 55° and 65° slope, respectively . It can be seen that $N_{br,d}$ agrees adequately with $N_{br,dyn}$ during the whole impact process for all tests. However, on each slope, an appropriate coefficient C_d must be chosen because the relative magnitude of inertial forces and gravity force on different slopes may not be similar (i.e. Froude number is different). In summary, the interaction forces between landslides and rigid barriers are composed of an earth pressure force caused by the weight of soil and a dynamic pressure force due to internal deformation (some sand mass is flowing on top of a growing dead zone). Neither part can be ignored if the impact force is correctly estimated. Additionally, the following equation is suitable for the whole interaction process.

$$N_{br} = K_w \rho g W S_{inter} + \frac{1}{2} C_d \rho v_{ave}^2 W l_{br,covered} \tag{13}$$

Engineers are more interested in the peak normal impact force $(N_{br})_{max}$. It is found in the previous section that when the normal impact force reaches the peak, the sand mass reaches the edge and $l_{br,covered}$ is the same as the run-up h_{run-up}. For granular materials, the cross-sectional area S_{inter} should be proportional to the square of the run-up (i.e. $S_{inter} = \chi h_{run-up}^2/2$). Take some special cases for example, for the final deposition presented in Figure 11 a, χ is $\tan(22° + 90° - \alpha_s)$. For deposited heaps formed by slowly pouring granular materials in front of the barrier, χ is $\tan(\text{AOR} + 90° - \alpha_s)$. χ is related to the friction angle ϕ_{crit} of the material and some dimensionless geometric parameters concerning the flow path and position of barriers. In the simple case studied in this paper, the dimensionless geometric parameter is the slope angle α_s. The peak normal impact force can then be expressed as

$$(N_{br})_{max} = (K_{earth} + C_d \frac{v_{ave}^2}{g h_{run-up}}) \frac{1}{2} \rho g W h_{run-up}^2 \tag{14}$$

Here, $K_{earth} = K_w \chi$ is the lateral earth coefficient, which is explained in Appendix 1. This equation is similar to the hydrostatic model, but the dynamic aspect is explicitly included in the empirical coefficient. $v_{ave}^2/g h_{run-up}$ is actually the square of the Froude number and therefore, the following model is proposed.

$$(N_{br})_{max} = [K_{earth} + C_d (Fr)^2] \frac{1}{2} \rho g W h_{run-up}^2 \tag{15}$$

When the flow is quasi-static, i.e. the inertia forces are extremely small compared with the gravity force ($Fr \ll 1$), the interaction force is the same as the lateral earth pressure force. For most cases, an increased earth pressure coefficient ($K_{earth} + C_d(Fr)^2$) depending on the Froude number should be used.

7 | CONCLUSIONS

This paper presents a study of the interaction between dry granular materials and rigid barriers using SPH simulations, where the granular materials are modelled as a rigid-perfectly plastic material with a Coulomb yield surface. Dilatancy is ignored and thus the material is assumed to be incompressible. The coupled continuity equation and momentum equations are solved using a semi-implicit algorithm.

The model is validated by carefully comparing its predictions with a series of flume experiments. In all cases, the model satisfactorily reproduces both the kinetic of flows, the impact force, as well as other flow features such as the development of the dead zone, the final deposition, etc.

A main contribution is the detailed study of the interaction process, which gives some insights into the physics and also practical conclusions are drawn, which might provide some guidelines for the design of debris-resisting barriers. The study reveals that the capacity of a debris-resisting basin is mainly determined by the head position of the barrier and the friction angle of the material. After quantitative examinations, it is illustrated that the impact force can be split into the earth pressure force caused by the weight of soil and the dynamic pressure force caused by internal deformation. Additionally, for the estimation of impact load, an increased earth pressure coefficient depending on the Froude number should be incorporated into the hydrostatic model.

ACKNOWLEDGEMENTS

The first author acknowledges the financial support from the Otto Pregl Foundation for Geotechnical Fundamental Research, Vienna, Austria and Jiangsu Province natural sciences fund subsidisation project (BK20170677). DL would like to thank the support from the European Union Seventh Framework Program (FP7/2007-2013) under grant agreement no. PIAG-GA-2012-324522 "MPM-DREDGE".

APPENDIX 1. EARTH PRESSURE FORCE

Taking the soil mass in the interaction zone as the object (Figure 14 a), we assume that the external soil mass (outside the interaction zone) has negligible interaction force with it (the two positions indicated in Figure 14 a). Therefore, the only external forces on the object are the interaction forces with the barrier and with the chute base. The interaction forces caused only by the weight (e.g. $N_{br,weight}$, $T_{br,weight}$, etc.) are in balance with the weight. The cross-sectional area of the mass is denoted as S_{inter}. Therefore, the weight is:

$$G = \rho g W S_{inter} \tag{16}$$

The equilibrium equations in the horizontal direction and in the vertical directions are:

$$-T_{br,weight}\sin\alpha_s - N_{br,weight}\cos\alpha_s - T_{ch,weight}\cos\alpha_s + N_{br,weight}\sin\alpha_s = 0 \tag{17}$$

$$-T_{br,weight}\cos\alpha_s + N_{br,weight}\sin\alpha_s + T_{ch,weight}\sin\alpha_s + N_{br,weight}\cos\alpha_s - G = 0 \tag{18}$$

Defining $T_{br,weight}/N_{br,weight}$ as $\tan\phi_{br,weight}$ and $T_{ch,weight}/N_{ch,weight}$ as $\tan\phi_{ch,weight}$, $N_{br,weight}$ could be solved from the equations above as

$$\begin{aligned} N_{br,weight} &= K_w \rho g W S_{inter} \\ K_w &= \frac{\sin(\alpha_s - \phi_{ch,wehigt})\cos\phi_{br,weight}}{\cos(\phi_{ch,wehigt} + \phi_{br,weight})} \end{aligned} \tag{19}$$

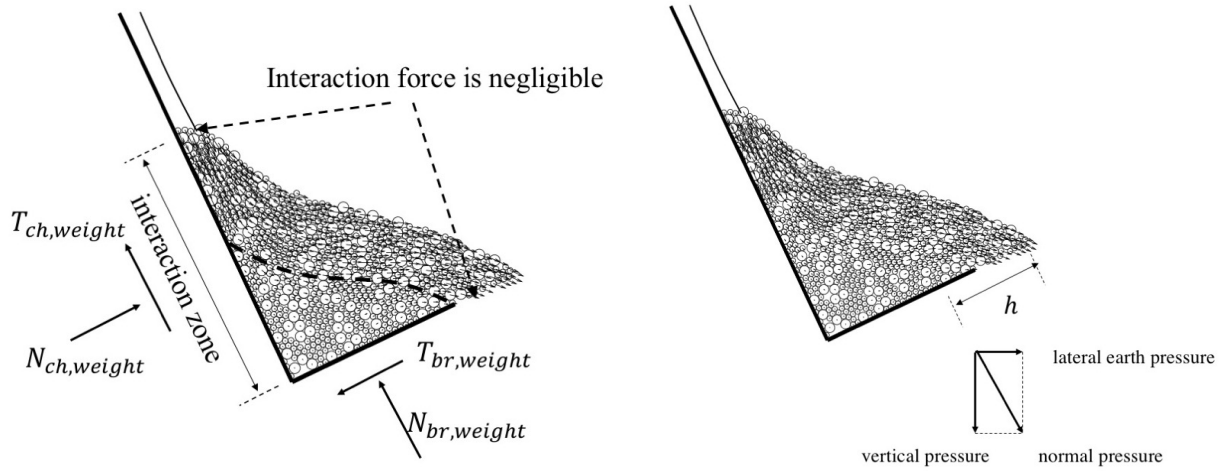

FIGURE 14 Interaction forces caused by the weight.

When the normal impact force reaches its peak, the cross-sectional area S_{inter} is proportional to the square of the run-up (i.e. $S_{inter} = \chi h_{run-up}^2/2$) and

$$N_{br,weight} = K_w \chi \rho g W h_{run-up}^2/2 \tag{20}$$

Consider a point on the barrier at a distance h from the free surface (Figure 14 b), the vertical pressure is $\rho g h \cos\alpha_s$. If the lateral earth coefficient is denoted as K_{earth}, the lateral earth pressure is $K_{earth}\rho g h \cos\alpha_s$ and the normal pressure is $K_{earth}\rho g h$. The integration along the barrier direction leads to the following equation.

$$N_{br,weight} = K_{earth} \rho g W h_{run-up}^2/2 \tag{21}$$

Comparing Equation 20 with Equation 21, we have $K_{earth} = K_w \chi$.

References

[1] A. Armanini and M. Michiue. Recent Developments on Debris Flows. Springer Berlin Heidelberg, 1997.

[2] L. Bugnion, B. W. McArdell, P. Bartelt, and C. Wendeler. Measurements of hill- slope debris flow impact pressure on obstacles. Landslides, 2011(9):179-187, 2012. doi: 10.1007/s10346-011-0294-4.

[3] D. Lo. Review of natural terrain landslide debris-resisting barrier design, Government of the Hong Kong Special Administrative Region, 2000.

[4] Y. J. Jiang and I. Towhata. Experimental study of dry granular flow and impact behavior against a rigid retaining wall. Rock Mechanics and Rock Engineering, 46(4):713-729, 2013. doi: 10.1007/s00603-012-0293-3.

[5] H. Teufelsbauer, Y. Wang, S. P. Pudasaini, R. I. Borja, and W. Wu. DEM simulation of impact force exerted by granular flow on rigid structures. Acta Geotechnica, 6(3):119-133, 2011. doi: 10.1007/s11440-011-0140-9.

[6] S. Moriguchi, R. I. Borja, A. Yashima, and K. Sawada. Estimating the impact force generated by granular flow on a rigid obstruction. Acta Geotechnica, 4 (1):57-71, 2009. doi: 10.1007/s11440-009-0084-5.

[7] E. J. Fern and K. Soga. The role of constitutive models in MPM simulations of granular column collapses. Acta Geotechnica, 11(3):659-678, jun 2016. doi: 10.1007/s11440-016-0436-x.

[8] P. A. Becker and S. R. Idelsohn. A multiresolution strategy for solving landslides using the Particle Finite Element Method. Acta Geotechnica, 11(3):643-657, jun 2016. doi: 10.1007/s11440-016-0464-6.

[9] H. Bui, R. Fukagawa, K. Sako, and J. Wells. Slope stability analysis and discontinuous slope failure simulation by elasto-plastic smoothed particle hydrodynamics (SPH). Geotechnique, 61(7):565-574, jul 2011. doi: 10.1680/geot.9.P.046.

[10] H. H. Bui, R. Fukagawa, K. Sako, and S. Ohno. Lagrangian meshfree particles method (SPH) for large deformation and failure flows of geomaterial using elastic-plastic soil constitutive model. International Journal for Numerical and Analytical Methods in Geomechanics, 32(12):1537-1570, aug 2008. doi: 10.1002/nag.688.

[11] C. Peng, X. Guo, W. Wu, and Y. Wang. Unified modelling of granular media with Smoothed Particle Hydrodynamics. Acta Geotechnica, pages 1231-1247, 2016. doi: 10.1007/s11440-016-0496-y.

[12] W. Zhang, K. Maeda, H. Saito, Z. Li, and Y. Huang. Numerical analysis on seepage failures of dike due to water level-up and rainfall using a water soil coupled smoothed particle hydrodynamics model. Acta Geotechnica, 11(6): 1401-1418, 2016. doi: 10.1007/s11440-016-0488-y.

[13] S. McDougall and O. Hungr. A model for the analysis of rapid landslide motion across three-dimensional terrain. Canadian Geotechnical Journal, 41(6):1084-1097, 2004. doi: 10.1139/t04-052.

[14] X. He, D. Liang, and M. D. Bolton. Run-out of cut-slope landslides: mesh-free simulations. Geotechnique, 68(1):50-63 . doi: 10.1680/jgeot.16.P.221.

[15] X. He and D. Liang. Study of the runout of granular columns with SPH methods. International Journal of Offshore and Polar Engineering, 25(4):281-287, dec 2015. doi: 10.17736/ijope.2015.ak06.

[16] X. He. SPH study of flow-type landslides and their interaction with rigid barriers. PhD thesis, Department of Engineering, University of Cambridge, UK, 2016.

[17] W. Wu, J. Lin, and X. Wang. A basic hypoplastic constitutive model for sand. Acta Geotechnica, 2017. doi: 10.1007/s11440-017-0550-4.

[18] M. D. Bolton. The strength and dilatancy of sands. Geotechnique, 36(1):65-78, 1986. doi: 10.1680/geot.1986.36.1.65.

[19] R. L. Michalowski. Stability of intact slopes with tensile strength cut-off. Geotechnique, 67(8):720-727, aug 2017. doi: 10.1680/jgeot.16.P.037.

[20] A. Schofield and P. Wroth. Critical state soil mechanics. McGraw-Hill, 1968.

[21] S. Bandara and K. Soga. Coupling of soil deformation and pore fluid flow using material point method. Computers and Geotechnics, 65:302, 2015. doi: 10.1016/j.compgeo.2014.12.007.

[22] J. Monaghan. Smoothed Particle Hydrodynamics and Its Diverse Applications. Annual Review of Fluid Mechanics, 44(1):323-346, 2012. doi: 10.1146/annurev-fluid-120710-101220.

[23] M. B. Liu and G. R. Liu. Smoothed particle hydrodynamics (SPH): An overview and recent developments. Archives of Computational Methods in Engineering, 17(1):25-76, 2010. doi: 10.1007/s11831-010-9040-7.

[24] H. Wendland. Piecewise polynomial, positive definite and compactly supported radial functions of minimal degree. Advances in Computational Mathematics, 4(1):389-396, 1995. doi: 10.1007/BF02123482.

[25] S. Shao. Incompressible smoothed particle hydrodynamics simulation of multi- fluid flows. International Journal for Numerical Methods in Fluids, 69(11): 1715-1735, aug 2012. doi: 10.1002/fld.2660.

[26] P. Randles and L. Libersky. Smoothed Particle Hydrodynamics: Some recent improvements and applications. Computer Methods in Applied Mechanics and Engineering, 139(1-4):375-408, dec 1996. doi: 10.1016/S0045-7825(96)01090- 0.

[27] J. Ai, P. A. Langston, and H.-S. Yu. Discrete element modelling of material non-coaxiality in simple shear flows. International Journal for Numerical and Analytical Methods in Geomechanics, 38(6):615-635, apr 2014. doi: 10.1002/nag.2230.

[28] L. Lacaze and R. R. Kerswell. Axisymmetric granular collapse: a transient 3D flow test of viscoplasticity. Physical Review Letters, 102(10):108305, mar 2009. doi: 10.1103/PhysRevLett.102.108305.

[29] J. M. N. T. Gray, Y.-C. Tai, and S. Noelle. Shock waves, dead zones and particle free regions in rapid granular free-surface flows. Journal of Fluid Mechanics, 491:S0022112003005317, 2003. doi: 10.1017/S0022112003005317.

[30] M. D. Bolton. A guide to soil mechanics. Macmillan, London, 1979.

[31] C. E. Choi, S. C. H. Au-Yeung, C. W. W. Ng, and D. Song. Flume investigation of landslide granular debris and water runup mechanisms. Geotechnique Letters, 5(1):28-32, jan 2015. doi: 10.1680/geolett.14.00080.

[32] C. Ng, D. Song, C. Choi, L. Liu, J. Kwan, R. Koo, and W. Pun. Impact mechanisms of granular and viscous flows on rigid and flexible barriers. Canadian Geotechnical Journal, 54(2):188-206, 2017. doi: 10.1139/cgj-2016-0128.

[33] Shao, S. and Lo, E. Y. M. (2003) Incompressible SPH method for simulating Newtonian and non-Newtonian flows with a free surface, Advances in Water Resources, 26(7), pp. 787-800. doi: 10.1016/S0309-1708(03)00030-7.

[34] Khayyer, A., Gotoh, H. and Shao, S. (2009) Enhanced predictions of wave impact pressure by improved incompressible SPH methods, Applied Ocean Research. Elsevier Ltd, 31(2), pp. 111-131. doi: 10.1016/j.apor.2009.06.003.

[35] Liang, D. and He, X. (2014) A comparison of conventional and shear-rate dependent Mohr-Coulomb models for simulating landslides, Journal of Mountain Science, 11(6), pp. 1478-1490. doi: 10.1007/s11629-014-3041-1.